





Article

Comparative Analysis of Raman Signal Amplifying Effectiveness of Silver Nanostructures with Different Morphology

Dzmitry V. Yakimchuk ^{1,*}, Soslan A. Khubezhov ^{2,3,4}, Uladzislau V. Prigodich ¹, Daria I. Tishkevich ^{1,5}, Sergei V. Trukhanov ^{1,6}, Alex V. Trukhanov ^{1,6}, Vladimir Sivakov ⁷ and Egor Y. Kaniukov ⁶

¹ Scientific-Practical Materials Research Centre of NAS of Belarus, 19 St. P.Brovka, 220072 Minsk, Belarus

² Southern Federal University, 2 St. Shevchenko, 347922 Taganrog, Russia

³ ITMO University, 9 St. Lomonosova, 191002 St. Petersburg, Russia

⁴ North Ossetian State University, 44-46 St. Vatutina, 362025 Vladikavkaz, Russia

⁵ Laboratory of Single Crystal Growth, South Ural State University, 454080 Chelyabinsk, Russia

⁶ Department of electronic Materials technology, National University of Science and Technology MISiS, 119049 Moscow, Russia

⁷ Leibniz Institute of Photonic Technology, Albert-Einstein Str. 9, 07745 Jena, Germany

* Correspondence: dim2yakim@gmail.com

Abstract: To increase the attractiveness of the practical application of molecular sensing methods, the experimental search for the optimal shape of silver nanostructures allowing to increase the Raman cross section by several orders of magnitude is of great interest. This paper presents a detailed study of spatially separated plasmon-active silver nanostructures grown in SiO₂/Si template pores with crystallite, dendrite, and “sunflower-like” nanostructures shapes. Nile blue and 2-mercaptobenzothiazole were chosen as the model analytes for comparative evaluation of the Raman signal amplification efficiency using these structures. It was discussed the features of the structures for the enhancement of Raman intensity. Finally, we showed that silver crystals, dendrites, and “sunflower-like” nanostructures in SiO₂/Si template could be used as the relevant materials for Raman signal amplification, but with different efficiency.

Keywords: silver; nanostructures; plasmonics; porous template; crystals; dendrites; SERS



Citation: Yakimchuk, D.V.; Khubezhov, S.A.; Prigodich, U.V.; Tishkevich, D.I.; Trukhanov, S.V.; Trukhanov, A.V.; Sivakov, V.; Kaniukov, E.Y. Comparative Analysis of Raman Signal Amplifying Effectiveness of Silver Nanostructures with Different Morphology. *Coatings* **2022**, *12*, 1419. <https://doi.org/10.3390/coatings12101419>

Academic Editor: Angela De Bonis

Received: 1 September 2022

Accepted: 22 September 2022

Published: 28 September 2022

Publisher's Note: MDPI stays neutral with regard to jurisdictional claims in published maps and institutional affiliations.



Copyright: © 2022 by the authors. Licensee MDPI, Basel, Switzerland. This article is an open access article distributed under the terms and conditions of the Creative Commons Attribution (CC BY) license (<https://creativecommons.org/licenses/by/4.0/>).

1. Introduction

Currently, there is an active search for express methods of the detection and analysis of molecular substances, which is necessary for such fields as pharmaceuticals [1–3], food quality control [4–7], and environmental pollution assessment [8–14]. One of the most popular express methods for studying molecular objects is Raman spectroscopy, which has a number of advantages: the possibility of studying substances in different aggregate states (solid, liquid, and gaseous), non-destructive testing, study of samples of different shapes, etc. However, this method is not suitable for the analysis of substances in low concentrations (from 10^{−4} M or less), because Raman spectroscopy has a low scattering cross section: 10^{−25}–10^{−30} cm^{−2}. This drawback can be eliminated by using nanostructured surfaces made of coin metals [11–14]: copper [15–18], silver [19–21], and gold [22–24]. Being near such a nanostructure, the molecule under study under the influence of external radiation from a laser with visible or infrared wavelengths experiences an instantaneous increase in the scattering cross-section due to a local increase in the electric field strength at the nanostructure boundaries [25–28]. These regions are called “hot spots”. The electric field strength at the “hot spots” depends on such parameters as the metal type size, shape of the nanostructure, and thr [25,29–33]. Among these metals, silver should be highlighted, because nanostructures made of this element allow a more effective amplification of the

Raman signal compared to those made of copper and gold [34]. This method of Raman signal amplification is called surface-enhanced Raman spectroscopy (SERS).

In a number of works, using various theoretical models and simulations, scientists have tried to show the optimal morphology of silver nanostructures for Raman signal amplification [35–38]. However, theoretical models do not always take into account the features of real nanostructures realized in practice. From this point of view, the study of silver nanostructures with different morphologies realized on the same substrate is of great interest. Understanding this, it is possible to demonstrate, using a simple experiment, which shape of nanostructures will be optimal for Raman signal amplification. Considering that such an approach will already predetermine the modes of nanostructures formation, the results of such an experiment will be of great importance for the subsequent practical implementation.

Among the general methods for obtaining nanostructures, three main directions can be distinguished [39]: metal nanoparticle assembly and bottom-up lithography, top-down lithography, and non-lithography techniques [40]. Metal nanoparticle assembly and bottom-up lithography usually includes methods such as direct self-assembly of metal nanoparticles [41], colloidal lithography [42], and block copolymer lithography [43]. Top-down lithography usually has three main branches: electron beam lithography [44], nanoimprint lithography [45], and laser interference lithography [46]. The non-lithographic techniques also have no one way to obtain silver nanostructures, for instance, hydrothermally roughened metal templates [47], hybrid methods of random hot-spot generation [48], maskless templates [49,50], etc. It should be noted that interesting highly ordered silver nanostructures were investigated in [51]. The authors obtained sunflower-like structures with dendrites on the edges. They used integrating deep-ultraviolet photolithography and electrodeposition method for the fabrication of the structures. Unfortunately, deep-ultraviolet lithography is a very expensive technique because of the complex optic system, which is necessary for focusing X-rays on the target substrate.

Among the variety of methods, due to their simplicity and high repeatability of the results, the method of controlled formation of silver nanostructures in a limited volume of silicon oxide pores on a silicon substrate should be highlighted. The limited pore volume determines the direction of adatom movement in the near-electrode layer, which allows controlling the self-assembly process by directing it in the desired direction. Thus, by changing the pore volume, the shape of nanostructures can be changed over a wide range. We previously demonstrated the effectiveness of this approach in creating structures with complex morphologies of copper [18], silver [52], and gold nanostructures [23,24] in the pores of SiO₂/Si matrices. We also showed that by varying the pore diameter, the morphology of the nanostructures can be changed over a wide range, and three morphologies should be distinguished as a main types of silver nanostructures: crystallites, dendrites, “sunflower-like” structures [53]. Other possible forms of silver nanostructures formed in the pores of SiO₂/Si templates are intermediate variants of the mentioned morphologies.

This work demonstrates the possibility of using the method of growing silver nanostructures in a limited volume of silicon oxide pores on a silicon substrate for controlled formation of silver nanostructures with the morphology of crystallites, dendrites, and “sunflower-like” structures. A detailed analysis of their morphology, composition, and structural features was carried out as well as a comparative analysis of their efficiency in the Raman signal amplification using the Nile Blue (NB, C₂₀H₂₀ClN₃O) dye molecule as an analyte.

2. Materials and Methods

Template formation. As templates for the synthesis of silver dendrites, swift heavy ion-track porous SiO₂ template on *p*-type silicon substrate (12 Ω·cm with the silicon crystal <100>) orientation was used. Latent ion tracks in the SiO₂ layer were formed using irradiation facilities at the cyclotron DC-60 (Astana, Kazakhstan). SiO₂/Si surfaces were bombarded at normal incidence with ²⁰⁸Bi ions with an energy of 1.75 MeV/nucleon. The

ion energy provided the guaranteed pulling through the silicon dioxide layer with a slight change in the electronic loss energy $(dE/dx)_e$. The irradiation fluence was chosen so as to avoid the spatial overlap of the individual pores appearing after etching of latent tracks in the SiO_2 matrix. The selected value for the fluence was $5 \times 10^7 \text{ cm}^{-2}$. The irradiated surfaces were cleaned in a solution of 56% HNO_3 at 80°C for 5 min, rinsed in deionized water, and then dried in flowing nitrogen. Subsequently, the surfaces were etched in 1 vol% aqueous hydrofluoric acid (HF) solutions for 48, 128, and 160 minutes at room temperature. The etching time was chosen to obtain pores with a diameter of approximately 320, 800, and 1000 nm, respectively. The selection of the etching conditions for obtaining pores with predetermined characteristics is described in detail in our work [54]. After etching, the samples were immediately washed in deionized water and then dried in flowing nitrogen. The parameters (Figure 1) of the porous template were determined by ellipsometry [55,56]. The pore density of SiO_2/Si on the surface was found to be $5 \times 10^7 \text{ cm}^{-2}$ according to the SEM studies determined with ImageJ [57].

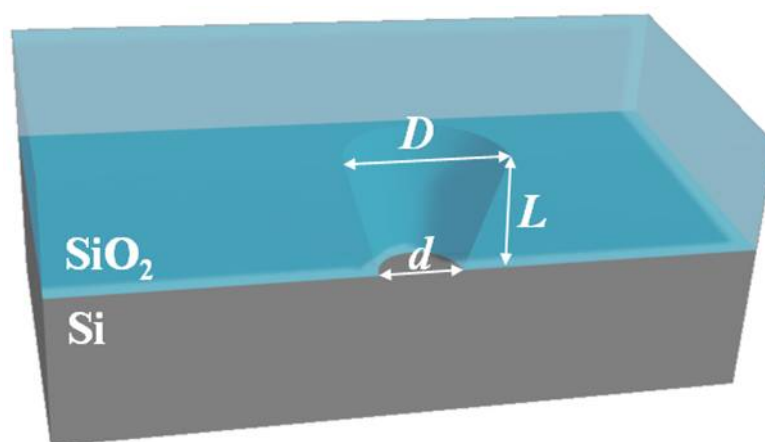


Figure 1. Schematic representation of a pore in a SiO_2/Si template (upper diameter D , lower diameter d , and thickness of silicon oxide layer L).

Synthesis of nanostructures. To localize silver in the pores of the amorphous silicon dioxide template the method of galvanic replacement was used [58]. Deposition was carried out by immersing SiO_2/Si templates with specified pore parameters (Table 1) in an aqueous solution containing 0.01 M silver nitrate (AgNO_3) and 5 M hydrofluoric acid (HF). The temperature of 35°C was set and controlled using a water bath, in which the electrolyte was incubated for 30 min before the deposition. The growth time was 40 s.

Table 1. Characteristic pore sizes in the SiO_2 layer used to obtain silver nanostructures.

D , nm	d , nm	L , nm
320 ± 12	0 ± 13	493 ± 19
800 ± 28	695 ± 27	163 ± 7
1000 ± 35	980 ± 33	26 ± 4

Structural study. The morphology and energy dispersive X-ray (EDX) analysis of the $\text{SiO}_2(\text{Ag})/\text{Si}$ surface was studied using JEOL JSM-7000F (Brussels, Belgium) and Carl Zeiss ULTRA 55 field emission scanning electron microscopes (FESEM) (Jena, Germany). X-ray diffraction (XRD) patterns were measured using X'Pert Pro X-ray diffractometer from PANalytical B.V. in the Bragg–Brentano arrangement.

Raman and SERS study. Plasmonic-active $\text{SiO}_2(\text{Ag})/\text{Si}$ substrates were incubated for 15 min in a solution of the analytes with a concentration of 10^{-6} M. The experiment was carried out at room temperature using 3D Scanning Laser Raman Spectrometer Confotec MR350 (SOL Instruments, Minsk, Belarus) with a confocal microscope for precise posi-

tioning of the laser beam. A solid-state diode green laser with a wavelength of 532 nm was used as an excitation source. The beam was focused using a 40× lens. The diameter of the resulting beam was ~1 μm. The spectrum acquisition time was 10 s. Spectra were recorded using a cooled CCD camera and a 600 lines/mm diffraction grating, achieving a resolution of 3 cm⁻¹. The available range of the laser power is 10 μW–3.5 mW. Raman and SERS spectra were obtained at laser powers of 3 mW and 60 μW, respectively. The power difference is due to the impossibility of obtaining a Raman spectrum with sufficient resolution and intensity at a power of 60 μW to determine the analyte molecule. On the contrary, in SERS measurements, a power of more than 60 μW leads to the destruction of the substance under study. It is also necessary to take into account the fact that the influence of the laser power has an ambiguous effect due to the random location of “hot spots” on plasmonic nanostructures. Therefore, when estimating the enhancement factor (EF), we will not consider changing in the laser power during Raman and SERS measurements. Thus, the values for EF given in the next section are “lower estimates”, but the actual values may be higher.

3. Results and Discussion

The variety of the morphology of silver nanostructures formed in the pores of SiO₂/Si templates is shown in the characteristic SEM images (Figure 2).

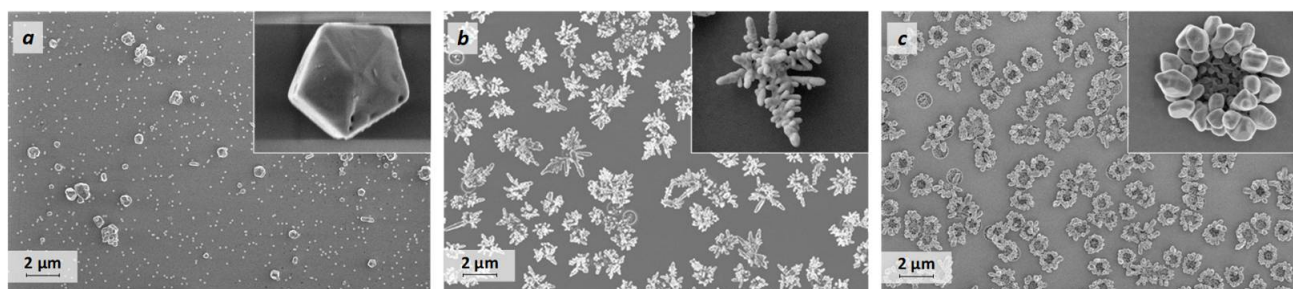


Figure 2. SEM planar images of silver nanostructures grown in SiO₂ pores with diameters D at the moment of pore opening (320 nm) (a); 800 nm (b); 1000 nm (c). The insets to the figures show enlarged images of structures with morphology typical for the selected deposition regimes.

As can be seen, crystallites are formed at the upper pore diameters of 320 nm, which corresponds to the moment of pore opening (Figure 2a). The most branched silver nanostructures, dendrites, are realized at $D = 800$ nm (Figure 2b). When the top diameter reaches 1000 nm and the oxide thickness is minimal, a “sunflower-like” structure is formed (Figure 2c). EDX analysis was performed to define the composition of the obtained structures (Figure 3).

EDX analysis of the samples showed the presence of silver, oxygen, and silicon elements, which are related with the structure and template, respectively. To demonstrate the absence of other elements, we present the EDX-spectrum together with the mapping of the studied surface of the silver crystallite (Figure 3a), dendrite (Figure 3b), and “sunflower-like” structure (Figure 3c). The percentage of silver content in the EDX spectra is in the range of 2–10%, depending on the pore diameter of the template into which the deposition was carried out: a larger pore diameter corresponds to higher silver content. The maximum content is achieved in samples with dendritic and “sunflower-like” morphologies, which correlates well with the visual representation according to SEM study. Features of the crystal structure of the obtained silver nanostructures were studied by XRD (Figure 4).

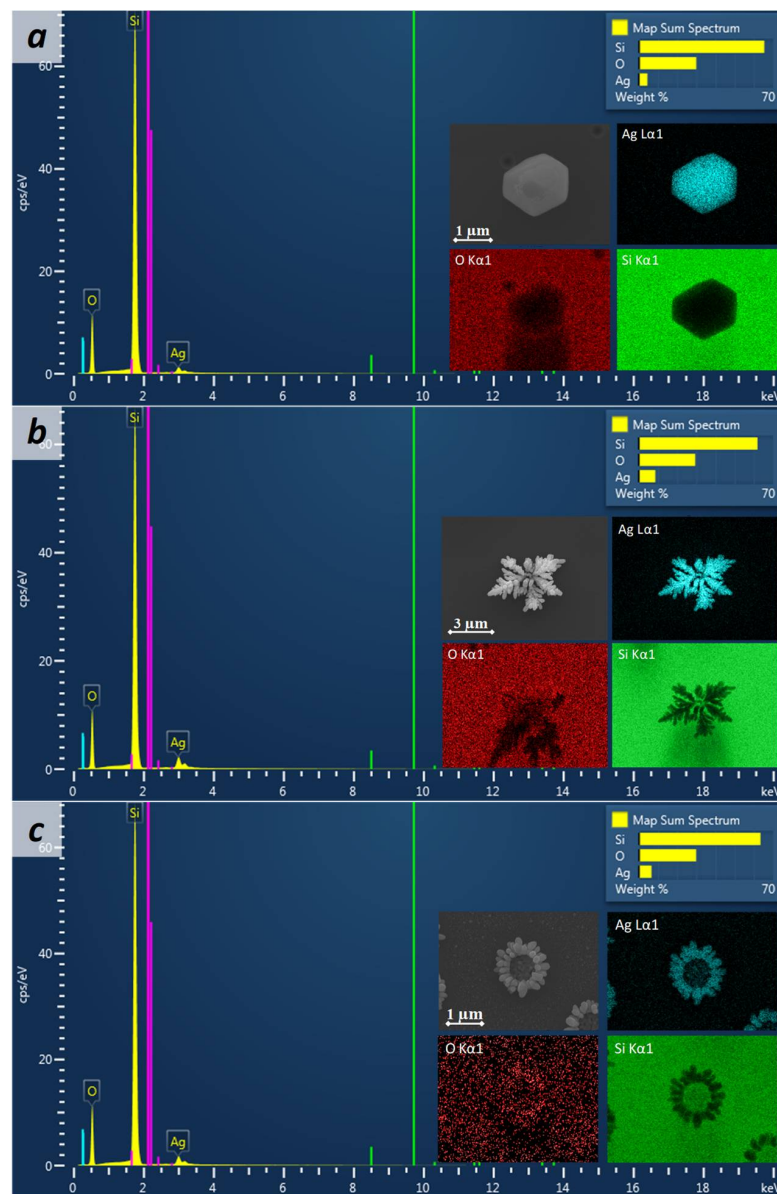


Figure 3. EDX-spectra, SEM and EDX maps of SiO₂(Ag)/Si with Ag crystal (a), dendrite (b), and “sunflower-like” (c) structures.

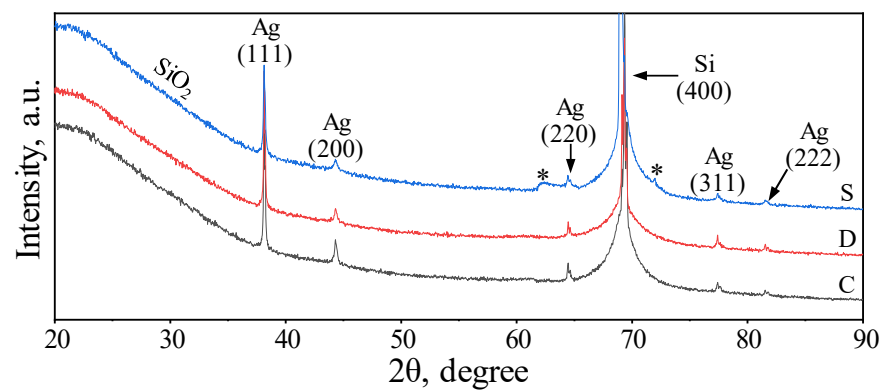


Figure 4. XRD patterns of SiO₂(Ag)/Si with different morphology of silver: (C, crystallites; S, “sunflowers”; D, dendrites).

The presence of the background halo is due to the signal from the amorphous SiO₂ template. All diffraction patterns exhibit peaks corresponding to silver reflections (111), (200), (220), (311), and (222), and the most intense line corresponding to the silicon plane (400) is additionally presented. On the X-ray diffraction pattern of the sample containing “sunflower-like” structures, indeterminate peaks marked with the symbol * were detected at the 2 theta values of 61–63° and 72°. Presumably, these peaks are related to the structurally altered state of the silicon surface caused by the influence of swift heavy ions during irradiation of the SiO₂/Si system at the stage of pore formation. In our opinion, the absence of these peaks on the X-ray diffraction patterns of other samples is a consequence of the fact that in the case of samples with crystallites and dendrites, the SiO₂ template pores are smaller in diameter and height. This reduces the penetrating power of X-rays and prevents the detection of subtle changes in the structure of the silicon surface, even in the signal acquisition mode for thin-film samples.

Crystallites, dendrites, and “sunflower-like” structures were evaluated for their use as plasmonic-active surfaces enhancing the Raman signal. Nile Blue dye (NB, C₂₀H₂₀ClN₃O) and 2-mercaptobenzothiazole (MBT, C₇H₅NS₂) were used as the test analytes in the experiment. Figures 5 and 6 show the Raman spectra obtained from the solid phase of substances as well as solutions (water solution for NB and ethanol solution for MBT) with the minimum concentration of analytes at which it is possible to distinguish their main characteristic peaks. For NB, these peaks are in the area of 590 cm⁻¹ (phenoxazine ring mode [59]) and 1600 cm⁻¹ (aromatic benzene ring breathing and stretching vibrations [60]). For MBT, they are in the area of 1380 cm⁻¹, which is combined with stretching of the NCS-ring, and peak 1240 cm⁻¹ relates to the C–S stretching modes [61], and in the area of 1589 cm⁻¹, which corresponds to C=C stretching [62]. Figures 5b and 6b have the spectra of the analytes with a concentration 10⁻⁶ M, which was also used for the next SERS investigations. It should be noted there are no molecular “fingerprints” there, only the background. Figure 5c–e for NB and Figure 6c–e for MBT show the mean SERS results of five spectra taken from different silver structures of the same type. The intensity values of the mean spectra for the lines under consideration are given in Table 2. The variation of intensity values is indicated in gray color in the graphs.

First consider SERS of NB. The resulting spectra are a set of lines characteristic of NB. Figure 5a, which corresponds to the SERS signal on the crystals, also contains a band between 930 cm⁻¹ and 1030 cm⁻¹ assigned in the literature to multi-phonon scattering generated in silicon substrate [63]. The spectra show that the intensity of the SERS signal obtained using crystallites is the lowest among the silver morphologies considered.

Next in order of increasing intensity are “sunflower-like” structures and dendrites. Based on the intensity values for the 590 cm⁻¹ line, the signal obtained using crystallites is 130 and 330 times weaker compared to the signal obtained using “sunflower-like” structures and dendrites, respectively. It should be noted that for the 1600 cm⁻¹ line, the same ratios have smaller values: 82 and 203. In Figure 5d, there is a noticeable statistical deviation in the region of 1150–1600 cm⁻¹, which is not observed in the spectra obtained on crystals and dendrites. This behavior may be due to the morphological features of “sunflower-like” structures, which consist of a greater number of random “hot spots” compared to crystallites and fewer compared to dendrites. Such “hot spots” are not distributed systematically, unlike crystallites (“hot spots” are usually located on the faces of crystals) and dendrites (“hot spots” are mainly concentrated at the base of dendrite branches) [52]. Table 3 has information about the *EF* for the 590 cm⁻¹ and 1600 cm⁻¹ Raman lines calculated using the formula given in [52]. As a result of comparing the spectra presented in Figure 5a,c–e we can conclude that the adsorption of NB molecules on plasmonic-active structures did not lead to a change in the chemical structure of the analyte.

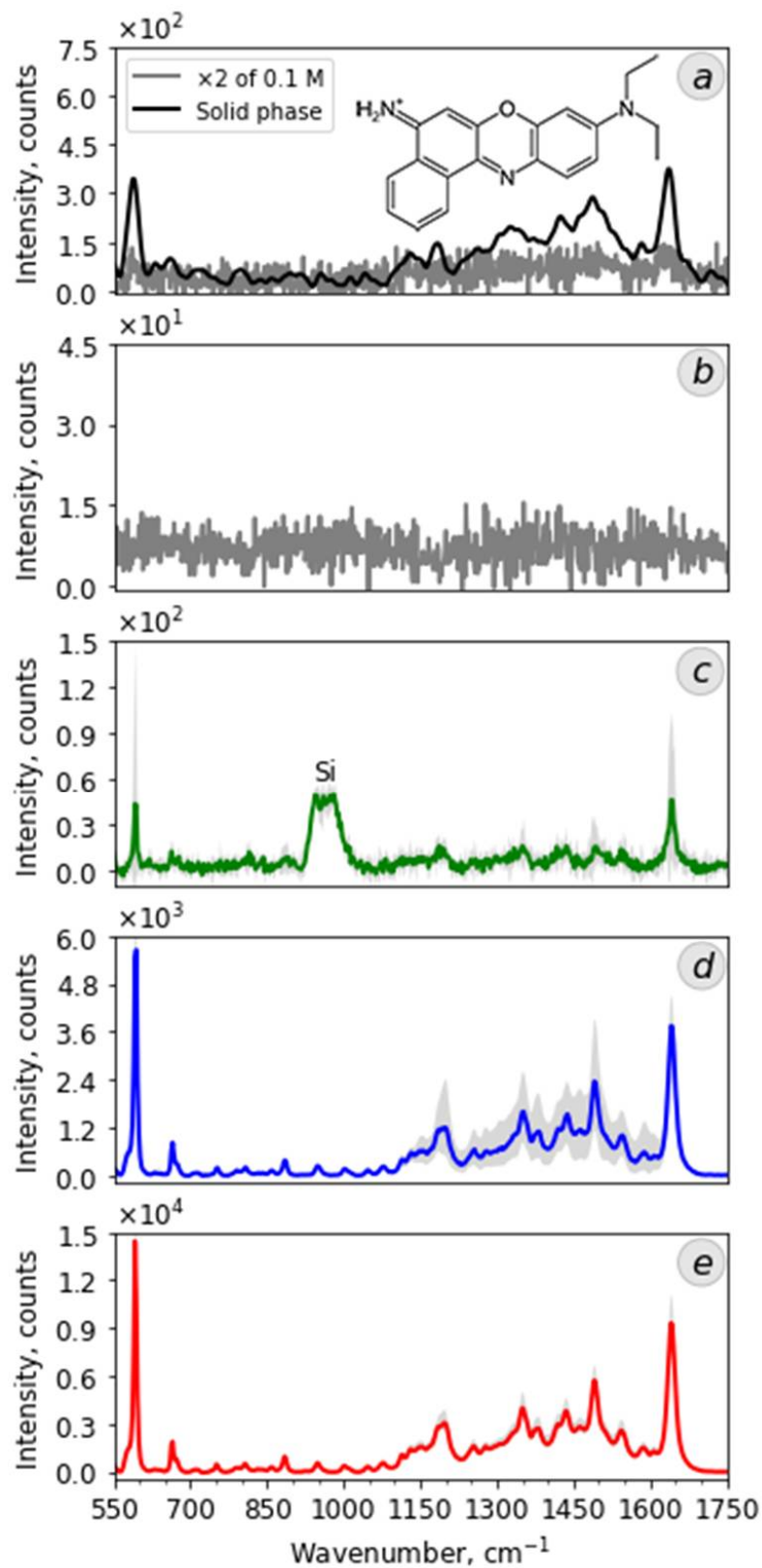


Figure 5. Raman spectra of NB ((a)—solid phase and 0.1 M, (b)— 10^{-6} M) and SERS (c–e) spectra of NB with a concentration of 10^{-6} M, obtained on the surface of silver nanostructures ((c), crystallites; (d), "sunflowers"; (e), dendrites) in the pores of the SiO_2/Si template.

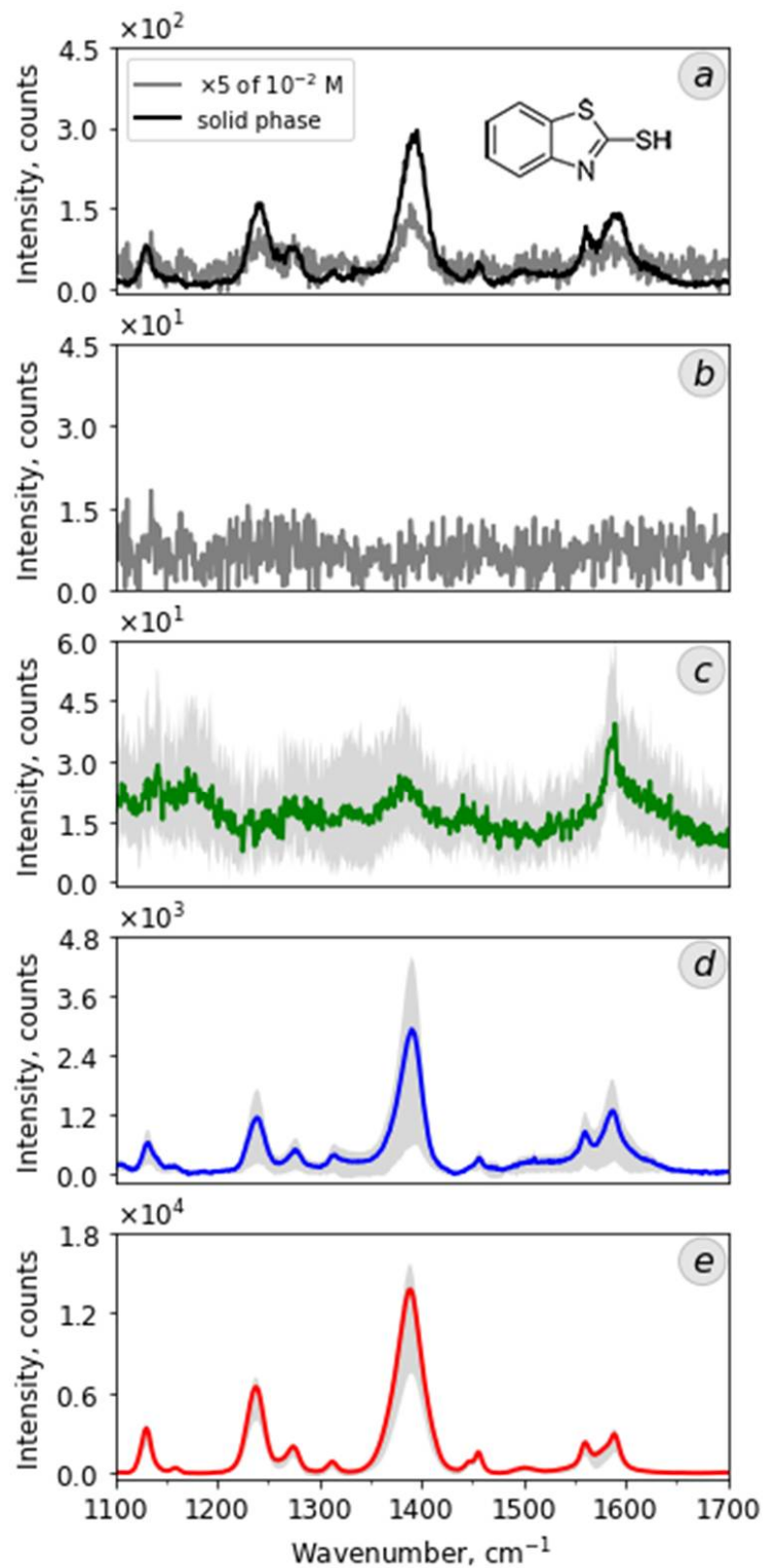


Figure 6. Raman spectra of MBT ((a)—solid phase and 10^{-2} M, (b)— 10^{-6} M) and SERS (c–e) spectra of MBT with a concentration of 10^{-6} M, obtained on the surface of silver nanostructures ((c), crystallites; (d) "sunflowers"; (e) dendrites) in the pores of the SiO_2/Si template.

Table 2. Intensity of characteristic lines for NB and MBT obtained by Raman and SERS methods.

Analyte Concentration, M	NB Line Intensity, Counts		MBT Line Intensity, Counts	
	590 cm ⁻¹	1600 cm ⁻¹	1380 cm ⁻¹	1589 cm ⁻¹
0.1–NB; 10 ⁻² –MBT	345	375	31	19
10 ⁻⁶ on crystals	43	46	39	27
10 ⁻⁶ on “sunflowers”	5648	3742	2909	1261
10 ⁻⁶ on dendrites	14,448	9329	13,734	2910

Table 3. EF of Raman lines for NB (590 cm⁻¹ и 1600 cm⁻¹) and MBT (1380 cm⁻¹ и 1589 cm⁻¹) molecules obtained using different type of silver nanostructures in SiO₂/Si template.

Type of Silver Nanostructures	NB		MBT	
	EF of 590 cm ⁻¹	EF of 1600 cm ⁻¹	EF of 1380 cm ⁻¹	EF of 1589 cm ⁻¹
Crystals	1.2 × 10 ⁴	1.2 × 10 ⁴	8.7 × 10 ³	2.1 × 10 ⁴
“Sunflowers”	1.6 × 10 ⁶	1.0 × 10 ⁶	9.4 × 10 ⁵	6.6 × 10 ⁵
Dendrites	4.4 × 10 ⁶	1.5 × 10 ⁶	4.3 × 10 ⁶	1.5 × 10 ⁶

Similar results were obtained using the MBT analyte. However, it is worth noting that the minimum concentration that could be registered using classical Raman spectroscopy was 10⁻² M. In addition, in Figure 6c, there is a feature in which the enhancement of the intensity of the 1589 cm⁻¹ line exceeds the intensity of the main line 1380 cm⁻¹. This indicates that, in the case of crystallites, the MBT molecule is adsorbed to the area of “hot spots” mainly by the C=C bond. In Table 2, the intensity values for the main characteristic lines of this molecule are given. EF values are presented in Table 3. As in the case of NB, according to the Raman signal amplification efficiency, the silver structures are in the following order: crystallites, “sunflower-like” structures, and dendrites, respectively.

Spatially separated dendritic Ag nanostructures in the pores of the SiO₂/Si ion-track template are expected to have the highest signal intensity. Our previous work [52] showed that Ag nanostructures shaped as dendrites have the ability to detect an ultra-low analyte concentration comparable to those of individual molecules. The high sensitivity of dendritic structures is associated with the presence of “hot spots” at twinning sites (coalescence of dendrite branches), and the electric field enhancement factor reaches 12. Random distribution of “hot spots” on the dendrite leads to the broadening of its scattering spectrum. Test results of SERS studies using SiO₂(Ag)/Si samples containing silver structures with different morphologies showed that the intensity of the received signal directly depends on the morphological features of the silver structures. It is important to note that these studies are only for demonstration purposes, while for each new analyte, a suitable morphology should be selected in order to avoid the destruction of its molecules. Given a simple method to obtain these structures with a wide choice of different morphologies by changing only one parameter (pore diameter of the SiO₂/Si template), a simple method for SERS studies of different types of analytes appears.

4. Conclusions

Thus, in this work, we performed a detailed study of three morphologies of silver structures obtained using template synthesis: crystallites, dendrites, and “sunflower-like” structures. X-ray diffraction of the samples including crystallites and dendrites agreed well with the tabular data, while X-ray diffraction of the sample with “sunflower-like” silver structures revealed an indefinite peak, which we attribute to the modification of the silicon substrate that appeared at the stage of irradiation during the creation of templates. Based on the study of low concentrations (10⁻⁶ M) of Nile Blue water solution and 2-mercaptobenzothiazole ethanol solution with the same concentration, the enhance-

ment factor for the main Raman lines (590 cm^{-1} and 1600 cm^{-1} for Nile Blue; 1380 cm^{-1} and 1589 cm^{-1} for 2-MBT) were determined. It was shown that dendrites, “sunflower” structures, and crystallites, respectively, have the Raman signal enhancement properties among the patterns in descending order. It was shown that crystallites amplify the signal relatively weakly (till 4 orders) due to the insufficient number of hot spots compared to other structures. It was revealed that the spectra obtained using “sunflower-like” structures have a noticeable statistical deviation in the Raman signal intensity, which is associated with the non-systematic distribution of “hot spots” over the structure surface. Nevertheless, the mean spectrum obtained on these structures makes it possible to achieve amplification more than six orders. The enhancement factor obtained using dendrites has also six orders, but higher than what the “sunflower-like” structures have. Thus, we can conclude that the considered structures could be used to amplify the Raman signal with varying degrees of efficiency.

Author Contributions: D.V.Y.: Conceptualization, Methodology, Investigation, Writing—original draft, Writing—review and editing, Supervision, Project administration. S.A.K.: Writing—original draft, Writing—review and editing. U.V.P.: Software, Writing—original draft, Writing—review and editing, Visualization. D.I.T.: Writing—original draft. S.V.T. and A.V.T.: Writing—original draft. V.S.: Conceptualization, Validation, Writing—original draft, Writing—review and editing, Supervision, Project administration. E.Y.K.: Conceptualization, Methodology, Investigation, Writing—review and editing, Supervision, Writing—original draft, Project administration. All authors have read and agreed to the published version of the manuscript.

Funding: The reported study was funded by Belarusian Foundation for Basic Research [project number $\Phi 21\text{PM-054}$], Scientific-technical program ‘Technology-SG’ [project number 3.1.5.1], RFBR and BRFBFBR project number 20-52-04015, and supported by the Ministry of Science and Higher Education of the Russian Federation; the state task in the field of scientific activity No. FENW-2022-0001.

Institutional Review Board Statement: Not applicable.

Informed Consent Statement: Not applicable.

Data Availability Statement: Data sharing is not applicable to this article.

Acknowledgments: The authors would like to thank the staff of the Research group Electrochemical and Surface Engineering of VUB for the technical support (SEM and EDX), especially Herman Terry, Jon Ustarroz, Priya Laha, and Kitty Baert.

Conflicts of Interest: The authors declare no conflict of interest. The funders had no role in the design of the study; in the collection, analyses, or interpretation of data; in the writing of the manuscript; or in the decision to publish the results.

References

1. Alula, M.T.; Mengesha, Z.T.; Mwenesongole, E. Advances in Surface-Enhanced Raman Spectroscopy for Analysis of Pharmaceuticals: A Review. *Vib. Spectrosc.* **2018**, *98*, 50–63. [[CrossRef](#)]
2. Frosch, T.; Knebl, A.; Frosch, T. Recent Advances in Nano-Photonic Techniques for Pharmaceutical Drug Monitoring with Emphasis on Raman Spectroscopy. *Nanophotonics* **2019**, *9*, 19–37. [[CrossRef](#)]
3. Caillaud, J.; De Bleye, C.; Dumont, E.; Sacré, P.-Y.; Netchacovitch, L.; Gut, Y.; Boiret, M.; Ginot, Y.-M.; Hubert, P.; Ziemons, E. Critical Review of Surface-Enhanced Raman Spectroscopy Applications in the Pharmaceutical Field. *J. Pharm. Biomed. Anal.* **2018**, *147*, 458–472. [[CrossRef](#)] [[PubMed](#)]
4. Adley, C. Past, Present and Future of Sensors in Food Production. *Foods* **2014**, *3*, 491–510. [[CrossRef](#)] [[PubMed](#)]
5. Zheng, J.; He, L. Surface-Enhanced Raman Spectroscopy for the Chemical Analysis of Food. *Compr. Rev. Food Sci. Food Saf.* **2014**, *13*, 317–328. [[CrossRef](#)] [[PubMed](#)]
6. Lin, Z.; He, L. Recent Advance in SERS Techniques for Food Safety and Quality Analysis: A Brief Review. *Curr. Opin. Food Sci.* **2019**, *28*, 82–87. [[CrossRef](#)]
7. Pavel, I.; Szeghalmi, A.; Moigno, D.; Cîntă, S.; Kiefer, W. Theoretical and PH Dependent Surface Enhanced Raman Spectroscopy Study on Caffeine. *Biopolymers* **2003**, *72*, 25–37. [[CrossRef](#)] [[PubMed](#)]
8. Li, D.-W.; Zhai, W.-L.; Li, Y.-T.; Long, Y.-T. Recent Progress in Surface Enhanced Raman Spectroscopy for the Detection of Environmental Pollutants. *Microchim. Acta* **2014**, *181*, 23–43. [[CrossRef](#)]

9. Halvorson, R.A.; Vikesland, P.J. Surface-Enhanced Raman Spectroscopy (SERS) for Environmental Analyses. *Environ. Sci. Technol.* **2010**, *44*, 7749–7755. [[CrossRef](#)]
10. Bodelón, G.; Pastoriza-Santos, I. Recent Progress in Surface-Enhanced Raman Scattering for the Detection of Chemical Contaminants in Water. *Front. Chem.* **2020**, *8*, 1–8. [[CrossRef](#)]
11. Sharma, B.; Frontiera, R.R.; Henry, A.-I.; Ringe, E.; Van Duyne, R.P. SERS: Materials, Applications, and the Future. *Mater. Today* **2012**, *15*, 16–25. [[CrossRef](#)]
12. Vinod, M.; Gopchandran, K.G. Au, Ag and Au:Ag Colloidal Nanoparticles Synthesized by Pulsed Laser Ablation as SERS Substrates. *Prog. Nat. Sci. Mater. Int.* **2014**, *24*, 569–578. [[CrossRef](#)]
13. Cheng, M.; Fang, J.; Cao, M.; Jin, Y. Surface-Enhanced Raman Scattering Dendritic Substrates Fabricated by Deposition of Gold and Silver on Silicon. *J. Nanosci. Nanotechnol.* **2010**, *10*, 7451–7454. [[CrossRef](#)]
14. Sun, X.; Lin, L.; Li, Z.; Zhang, Z.; Feng, J. Novel Ag–Cu Substrates for Surface-Enhanced Raman Scattering. *Mater. Lett.* **2009**, *63*, 2306–2308. [[CrossRef](#)]
15. Kudelski, A.; Janik-Czachor, M.; Bukowska, J.; Dolata, M.; Szummer, A. Surface-Enhanced Raman Scattering (SERS) on Copper Electrodeposited under Nonequilibrium Conditions. *J. Mol. Struct.* **1999**, *482–483*, 245–248. [[CrossRef](#)]
16. Wang, R.C.; Li, C.H. Cu, Cu–Cu₂O Core-Shell, and Hollow Cu₂O Nanodendrites: Structural Evolution and Reverse Surface-Enhanced Raman Scattering. *Acta Mater.* **2011**, *59*, 822–829. [[CrossRef](#)]
17. Shao, Q.; Que, R.; Shao, M.; Cheng, L.; Lee, S.-T. Copper Nanoparticles Grafted on a Silicon Wafer and Their Excellent Surface-Enhanced Raman Scattering. *Adv. Funct. Mater.* **2012**, *22*, 2067–2070. [[CrossRef](#)]
18. Kaniukov, E.; Yakimchuk, D.; Arzumanyan, G.; Terryn, H.; Baert, K.; Kozlovskiy, A.; Zdorovets, M.; Belonogov, E.; Demyanov, S. Growth Mechanisms of Spatially Separated Copper Dendrites in Pores of a SiO₂ Template. *Philos. Mag.* **2017**, *97*. [[CrossRef](#)]
19. Panarin, A.Y.; Terekhov, S.N.; Kholostov, K.I.; Bondarenko, V.P. SERS-Active Substrates Based on n-Type Porous Silicon. *Appl. Surf. Sci.* **2010**, *256*, 6969–6976. [[CrossRef](#)]
20. Sun, B.; Jiang, X.; Dai, S.; Du, Z. Single-Crystal Silver Nanowires: Preparation and Surface-Enhanced Raman Scattering (SERS) Property. *Mater. Lett.* **2009**, *63*, 2570–2573. [[CrossRef](#)]
21. Yakimchuk, D.; Kaniukov, E.; Bundyukova, V.; Osminkina, L.; Teichert, S.; Demyanov, S.; Sivakov, V. Silver Nanostructures Evolution in Porous SiO₂/p-Si Matrices for Wide Wavelength Surface-Enhanced Raman Scattering Applications. *MRS Commun.* **2018**, *8*. [[CrossRef](#)]
22. Cho, F.H.; Lin, Y.C.; Lai, Y.H. Electrochemically Fabricated Gold Dendrites with High-Index Facets for Use as Surface-Enhanced Raman-Scattering-Active Substrates. *Appl. Surf. Sci.* **2017**, *402*, 147–153. [[CrossRef](#)]
23. Yakimchuk, D.V.; Bundyukova, V.D.; Ustarroz, J.; Terryn, H.; Baert, K.; Kozlovskiy, A.L.; Zdorovets, M.V.; Khubezhov, S.A.; Trukhanov, A.V.; Trukhanov, S.V.; et al. Morphology and Microstructure Evolution of Gold Nanostructures in the Limited Volume Porous Matrices. *Sensors* **2020**, *20*, 4397. [[CrossRef](#)]
24. Osminkina, L.A.; Žukovskaja, O.; Agafilushkina, S.N.; Kaniukov, E.; Stranik, O.; Gonchar, K.A.; Yakimchuk, D.; Bundyukova, V.; Chermoshentsev, D.A.; Dyakov, S.A.; et al. Gold Nanoflowers Grown in a Porous Si/SiO₂ Matrix: The Fabrication Process and Plasmonic Properties. *Appl. Surf. Sci.* **2020**, *507*, 144989. [[CrossRef](#)]
25. Kim, S.; Jung, Y.; Gu, G.H.; Suh, J.S.; Park, S.M.; Ryu, S. Discrete Dipole Approximation Calculations of Optical Properties of Silver Nanorod Arrays in Porous Anodic Alumina. *J. Phys. Chem. C* **2009**, *113*, 16321–16328. [[CrossRef](#)]
26. Ding, S.-Y.; You, E.-M.; Tian, Z.-Q.; Moskovits, M. Electromagnetic Theories of Surface-Enhanced Raman Spectroscopy. *Chem. Soc. Rev.* **2017**, *46*, 4042–4076. [[CrossRef](#)]
27. Qiu, T.; Zhou, Y.; Li, J.; Zhang, W.; Lang, X.; Cui, T.; Chu, P.K. Hot Spots in Highly Raman-Enhancing Silver Nano-Dendrites. *J. Phys. D: Appl. Phys.* **2009**, *42*, 175403. [[CrossRef](#)]
28. Wang, A.; Kong, X. Review of Recent Progress of Plasmonic Materials and Nano-Structures for Surface-Enhanced Raman Scattering. *Materials* **2015**, *8*, 3024–3052. [[CrossRef](#)]
29. Shaw, C.P.; Fan, M.; Lane, C.; Barry, G.; Jirasek, A.I.; Brolo, A.G. Statistical Correlation between SERS Intensity and Nanoparticle Cluster Size. *J. Phys. Chem. C* **2013**, *117*, 16596–16605. [[CrossRef](#)]
30. Gellner, M.; Küstner, B.; Schlücker, S. Optical Properties and SERS Efficiency of Tunable Gold/Silver Nanoshells. *Vib. Spectrosc.* **2009**, *50*, 43–47. [[CrossRef](#)]
31. Willets, K.A.; Van Duyne, R.P. Localized Surface Plasmon Resonance Spectroscopy and Sensing. *Annu. Rev. Phys. Chem.* **2007**, *58*, 267–297. [[CrossRef](#)] [[PubMed](#)]
32. Jones, M.R.; Osberg, K.D.; MacFarlane, R.J.; Langille, M.R.; Mirkin, C.A. Templated Techniques for the Synthesis and Assembly of Plasmonic Nanostructures. *Chem. Rev.* **2011**, *111*, 3736–3827. [[CrossRef](#)] [[PubMed](#)]
33. Bamal, D.; Singh, A.; Chaudhary, G.; Kumar, M.; Singh, M.; Rani, N.; Mundlia, P.; Sehrawat, A.R. Silver Nanoparticles Biosynthesis, Characterization, Antimicrobial Activities, Applications, Cytotoxicity and Safety Issues: An Updated Review. *Nanomaterials* **2021**, *11*, 2086. [[CrossRef](#)] [[PubMed](#)]
34. Pérez-Jiménez, A.I.; Lyu, D.; Lu, Z.; Liu, G.; Ren, B. Surface-Enhanced Raman Spectroscopy: Benefits, Trade-Offs and Future Developments. *Chem. Sci.* **2020**, *11*, 4563–4577. [[CrossRef](#)] [[PubMed](#)]
35. Mandelbaum, Y.; Mottes, R.; Zalevsky, Z.; Zitoun, D.; Karsenty, A. Design of Surface Enhanced Raman Scattering (SERS) Nanosensor Array. *Sensors* **2020**, *20*, 5123. [[CrossRef](#)] [[PubMed](#)]

36. Solís, D.M.; Taboada, J.M.; Obelleiro, F.; Liz-Marzán, L.M.; García de Abajo, F.J. Optimization of Nanoparticle-Based SERS Substrates through Large-Scale Realistic Simulations. *ACS Photonics* **2017**, *4*, 329–337. [[CrossRef](#)]
37. Wei, S.; Zheng, M.; Xiang, Q.; Hu, H.; Duan, H. Optimization of the Particle Density to Maximize the SERS Enhancement Factor of Periodic Plasmonic Nanostructure Array. *Opt. Express* **2016**, *24*, 20613. [[CrossRef](#)]
38. Dutta, A.; Alam, K.; Nuutinen, T.; Hulkko, E.; Karvinen, P.; Kuitinen, M.; Toppari, J.J.; Vartiainen, E.M. Influence of Fano Resonance on SERS Enhancement in Fano-Plasmonic Oligomers. *Opt. Express* **2019**, *27*, 30031. [[CrossRef](#)]
39. Jeon, T.Y.; Kim, D.J.; Park, S.-G.; Kim, S.-H.; Kim, D.-H. Nanostructured Plasmonic Substrates for Use as SERS Sensors. *Nano Converg.* **2016**, *3*, 18. [[CrossRef](#)]
40. Tishkevich, D.I.; Vorobjova, A.I.; Bondaruk, A.A.; Dashkevich, E.S.; Shimanovich, D.L.; Razanau, I.U.; Zubar, T.I.; Yakimchuk, D.V.; Dong, M.G.; Sayyed, M.I.; et al. The Interrelation of Synthesis Conditions and Wettability Properties of the Porous Anodic Alumina Membranes. *Nanomaterials* **2022**, *12*, 2382. [[CrossRef](#)]
41. Shin, Y.; Song, J.; Kim, D.; Kang, T. Facile Preparation of Ultrasmall Void Metallic Nanogap from Self-Assembled Gold-Silica Core-Shell Nanoparticles Monolayer via Kinetic Control. *Adv. Mater.* **2015**, *27*, 4344–4350. [[CrossRef](#)]
42. Jeon, T.Y.; Park, S.-G.; Lee, S.Y.; Jeon, H.C.; Yang, S.-M. Shape Control of Ag Nanostructures for Practical SERS Substrates. *ACS Appl. Mater. Interfaces* **2013**, *5*, 243–248. [[CrossRef](#)]
43. Ouk Kim, S.; Solak, H.H.; Stoykovich, M.P.; Ferrier, N.J.; de Pablo, J.J.; Nealey, P.F. Epitaxial Self-Assembly of Block Copolymers on Lithographically Defined Nanopatterned Substrates. *Nature* **2003**, *424*, 411–414. [[CrossRef](#)]
44. Pasquale, A.J.; Reinhard, B.M.; Dal Negro, L. Concentric Necklace Nanolenses for Optical Near-Field Focusing and Enhancement. *ACS Nano* **2012**, *6*, 4341–4348. [[CrossRef](#)]
45. Ahn, S.H.; Guo, L.J. Large-Area Roll-to-Roll and Roll-to-Plate Nanoimprint Lithography: A Step toward High-Throughput Application of Continuous Nanoimprinting. *ACS Nano* **2009**, *3*, 2304–2310. [[CrossRef](#)]
46. Park, S.-G.; Jeon, T.Y.; Jeon, H.C.; Kwon, J.-D.; Mun, C.; Lee, M.; Cho, B.; Kim, C.S.; Song, M.; Kim, D.-H. Fabrication of Au-Decorated 3D ZnO Nanostructures as Recyclable SERS Substrates. *IEEE Sens. J.* **2016**, *16*, 3382–3386. [[CrossRef](#)]
47. Yamazoe, S.; Naya, M.; Shiota, M.; Morikawa, T.; Kubo, A.; Tani, T.; Hishiki, T.; Horiuchi, T.; Suematsu, M.; Kajimura, M. Large-Area Surface-Enhanced Raman Spectroscopy Imaging of Brain Ischemia by Gold Nanoparticles Grown on Random Nanoarrays of Transparent Boehmite. *ACS Nano* **2014**, *8*, 5622–5632. [[CrossRef](#)]
48. Park, S.-G.; Mun, C.; Lee, M.; Jeon, T.Y.; Shim, H.-S.; Lee, Y.-J.; Kwon, J.-D.; Kim, C.S.; Kim, D.-H. 3D Hybrid Plasmonic Nanomaterials for Highly Efficient Optical Absorbers and Sensors. *Adv. Mater.* **2015**, *27*, 4290–4295. [[CrossRef](#)]
49. Packed with Action. *Adv. Mater.* **2012**, *24*, 10–12. [[CrossRef](#)]
50. Shumskaya, A.; Korolkov, I.; Rogachev, A.; Ignatovich, Z.; Kozlovskiy, A.; Zdorovets, M.; Anisovich, M.; Bashouti, M.; Shalabny, A.; Busool, R.; et al. Synthesis of Ni@Au Core-Shell Magnetic Nanotubes for Bioapplication and SERS Detection. *Colloids Surfaces A Physicochem. Eng. Asp.* **2021**, *626*, 127077. [[CrossRef](#)]
51. Chu, J.; Zhao, Y.; Li, S.-H.; Li, W.-W.; Chen, X.-Y.; Huang, Y.-X.; Chen, Y.-P.; Qu, W.-G.; Yu, H.-Q.; Xu, A.-W.; et al. A Highly-Ordered and Uniform Sunflower-like Dendritic Silver Nanocomplex Array as Reproducible SERS Substrate. *RSC Adv.* **2015**, *5*, 3860–3867. [[CrossRef](#)]
52. Yakimchuk, D.V.; Kaniukov, E.Y.; Lepeshov, S.; Bundyukova, V.D.; Demyanov, S.E.; Arzumanyan, G.M.; Doroshkevich, N.V.; Mamatkulov, K.Z.; Bochmann, A.; Presselt, M.; et al. Self-Organized Spatially Separated Silver 3D Dendrites as Efficient Plasmonic Nanostructures for Surface-Enhanced Raman Spectroscopy Applications. *J. Appl. Phys.* **2019**, *126*. [[CrossRef](#)]
53. Yakimchuk, D.V.; Prigodich, U.V.; Demyanov, S.E.; Ustarroz, J.; Terryn, H.; Baert, K.; Khubezhov, S.A.; Tishkevich, D.I.; Trukhanov, A.V.; Sivakov, V.; et al. Growth Mechanism Study of Silver Nanostructures in a Limited Volume. *Mater. Chem. Phys.* **2022**, *283*, 126016. [[CrossRef](#)]
54. Kaniukov, E.Y.; Ustarroz, J.; Yakimchuk, D.V.; Petrova, M.; Terryn, H.; Sivakov, V.; Petrov, A.V. Tunable Nanoporous Silicon Oxide Templates by Swift Heavy Ion Tracks Technology. *Nanotechnology* **2016**, *27*. [[CrossRef](#)] [[PubMed](#)]
55. Bundyukova, V.; Kaniukov, E.; Shumskaya, A.; Smirnov, A.; Kravchenko, M.; Yakimchuk, D. Ellipsometry as an Express Method for Determining the Pore Parameters of Ion-Track SiO₂ Templates on a Silicon Substrate. *EPJ Web Conf.* **2019**, *201*, 01001. [[CrossRef](#)]
56. Yakimchuk, D.; Bundyukova, V.; Smirnov, A.; Kaniukov, E. Express Method of Estimation of Etched Ion Track Parameters in Silicon Dioxide Template. *Phys. Status Solidi* **2019**, *256*, 1800316. [[CrossRef](#)]
57. Bundyukova, V.; Yakimchuk, D.; Shumskaya, E.; Smirnov, A.; Yarmolich, M.; Kaniukov, E. Post-Processing of SiO₂/Si Ion-Track Template Images for Pores Parameters Analysis. *Mater. Today Proc.* **2019**, *7*, 828–834. [[CrossRef](#)]
58. Yan, M.; Xiang, Y.; Liu, L.; Chai, L.; Li, X.; Feng, T. Silver Nanocrystals with Special Shapes: Controlled Synthesis and Their Surface-Enhanced Raman Scattering Properties. *RSC Adv.* **2014**, *4*, 98–104. [[CrossRef](#)]
59. Sivakov, V.; Kaniukov, E.Y.; Petrov, A.V.; Korolik, O.V.; Mazanik, A.V.; Bochmann, A.; Teichert, S.; Hidi, I.J.; Schleusener, A.; Cialla, D.; et al. Silver Nanostructures Formation in Porous Si/SiO₂ Matrix. *J. Cryst. Growth* **2014**, *400*, 21–26. [[CrossRef](#)]
60. Michota, A.; Bukowska, J. Surface-Enhanced Raman Scattering (SERS) of 4-Mercaptobenzoic Acid on Silver and Gold Substrates. *J. Raman Spectrosc.* **2003**, *34*, 21–25. [[CrossRef](#)]
61. Song, C.; Wang, Z.; Yang, J.; Zhang, R.; Cui, Y. Preparation of 2-Mercaptobenzothiazole-Labeled Immuno-Au Aggregates for SERS-Based Immunoassay. *Colloids Surf. B Biointerfaces* **2010**, *81*, 285–288. [[CrossRef](#)]

-
62. Rai, A.K.; Singh, R.; Singh, K.N.; Singh, V.B. FTIR, Raman Spectra and Ab Initio Calculations of 2-Mercaptobenzothiazole. *Spectrochim. Acta Part A Mol. Biomol. Spectrosc.* **2006**, *63*, 483–490. [[CrossRef](#)]
 63. Temple, P.A.; Hathaway, C.E. Multiphonon Raman Spectrum of Silicon. *Phys. Rev. B* **1973**, *7*, 3685–3697. [[CrossRef](#)]